THE WIDE BAND SPECTROMETER ON THE SOLAR-A*

M. YOSHIMORI, K. OKUDAIRA, Y. HIRASIMA, T. IGARASHI,
M. AKASAKA,
Y. TAKAI, K. MORIMOTO

Rikkyo University, Toshima-ku, Tokyo 171, Japan

T. WATANABE, K. OHKI

National Astronomical Observatory, Mitaka, Tokyo 181, Japan

J. NISHIMURA, T. YAMAGAMI, Y. OGAWARA

Institute of Space and Astronautical Science, Sagamihara, Kanagawa 229, Japan

and

I. KONDO

Shibaura Institute of Technology, Ohmiya, Saitama 330, Japan

(Received 22 March, 1991; in revised form 17 May, 1991)

Abstract. The SOLAR-A spacecraft has spectroscopic capabilities in a wide energy band from soft X-rays to gamma-rays. The Wide Band Spectrometer (WBS), consisting of three kinds of spectrometers, soft X-ray spectrometer (SXS), hard X-ray spectrometer (HXS) and gamma-ray spectrometer (GRS), is installed on SOLAR-A to investigate plasma heating, high-energy particle acceleration, and interaction processes. SXS has two proportional counters and each counter provides 128-channel pulse height data in the 2–30 keV range every 2 s and 2-channel pulse count data every 0.25 s. HXS has a NaI scintillation detector and provides 32-channel pulse height data in the 20–400 keV range every 1 s and 2-channel pulse count data every 0.125 s. GRS has two identical BGO scintillation detectors and each detector provides 128-channel pulse height data in the 0.2–10 MeV range every 4 s and 4-channel pulse count data (0.2–0.7, 0.7–4, 4–7, and 7–10 MeV) every 0.25–0.5 s. In addition, each of the BGO scintillation detectors provides 16-channel pulse height data in the 8–100 MeV range every 4 s and 2-channel pulse count data (8–30 and 30–100 MeV) every 0.5 s. The SXS observations enable one to study the thermal evolution of flare plasma by obtaining time series of electron temperatures and emission measures of hot plasma; the HXS observations enable one to study the electron acceleration and heating mechanisms by obtaining time series of the electron spectrum; and the GRS observations enable one to study the high-energy electron and ion acceleration and interaction processes by obtaining time series of electron and ion spectra.

1. Scientific Objectives

The SMM and HINOTORI satellites observed a large number of flares in the 21st solar maximum in the early 1980s. New findings of magnetic energy release processes, plasma heating, and particle acceleration were reported. The detailed scientific results were presented in the following special issues: *Solar Phys.* **86** (1983), No. 1, *Solar Phys.* **111** (1987), No. 1, *Solar Phys.* **113** (1987), Nos. 1 and 2, *Solar Phys.* **118** (1988), Nos 1 and 2, *Space Sci. Rev.* **51** (1989), No. 1, and *Astrophys. J. Suppl.* **73** (1990). Some of the primary questions concerning these fundamentals of flare phenomena, however, still

* After the launch the name of SOLAR-A has been changed to YOHKOH.

Solar Physics **136:** 69–88, 1991.

remain unsolved. Attempts have been made to show how future observations with increased sensitivity and improved spatial and spectral resolutions will answer these questions. Explosive phenomena such as the solar flare are a common characteristic of cosmic plasma at many sites throughout the universe, and a detailed understanding of these high-energy processes is one of the major goals of astrophysics.

Spectroscopic observations in a wide energy band of soft X-rays to gamma-rays provide important clues to the plasma heating and particle acceleration processes. The soft X-ray spectrum consists of components of continuum and various lines. The emission in energies above 5 keV is mostly continuum which results from hot thermal plasma, with the exception of the strong line emission at 6.7 keV which results from excited iron ions. The electron temperature and emission measure of hot plasma can be derived from the soft X-ray continuum spectrum (e.g., Watanabe *et al.*, 1983). Further, the thermal energy content is calculated from these two parameters. The thermal evolution of the flare plasma can be studied with these temporally resolved quantities. The soft X-ray spectral observation diagnoses the hot flare plasma and provides complementary data for other experiments on board SOLAR-A: the soft X-ray telescope (SXT) and the Bragg crystal spectrometer (BCS).

The hard X-ray observation provides the most direct information for understanding the energy release processes and the electron acceleration mechanisms. The hard X-ray intensity variations correlate with electron acceleration. The onset of the hard X-ray emission gives the most important signal for the earliest time of the magnetic energy release. The electron acceleration and plasma heating mechanisms can be deduced from the temporal and spectral analyses of the hard X-ray emission (e.g., Dennis, 1988). The conditions at the energy release site, the magnetic field configuration, and the parameters of the flare plasma before, during, and after the flare are determined from coincident observations of images in both hard and soft X-rays and at other wavelengths.

The gamma-ray observations provide irreplaceable information for study of the highest-energy flare phenomena (Chupp, 1984, 1987; Yoshimori, 1989). The radiation in the gamma-ray range is emitted by several processes including high-energy electron bremsstrahlung, nuclear de-excitation, positron annihilation, neutron capture, and neutral pion decay. The electron bremsstrahlung produces a continuum spectrum extending to the maximum energy of the accelerated electrons. Thus the electron acceleration to the highest energies can be studied from the temporal and spectral analyses of the gamma-ray emission. The other gamma-ray emissions result from energetic ion interactions with the solar ambient medium. The detection of these gamma-ray emissions gives evidence of nuclear reactions at the flare site. The nuclear de-excitation produces a prompt line emission in the MeV energies. The nuclear de-excitation lines are mostly produced by ions accelerated to 10–30 MeV nucl^{-1}. The positrons are mostly emitted by beta-decay nuclei produced by 10–100 MeV nucl^{-1} ion interactions. The neutron capture on protons emits a delayed line at 2.22 MeV. The neutrons contributing to the 2.22 MeV line emission are produced by ions with energies < 100 MeV nucl^{-1}. The pion decay gamma-ray spectrum with a broad peak at 70 MeV is different from the high-energy electron bremsstrahlung spectrum. Since the pions are produced by protons

accelerated to energies > 1 GeV, the pion decay gamma-ray emission provides evidence of very high-energy proton acceleration. High-energy neutron observation also provides similar evidence. The high-energy electron and ion acceleration processes are investigated from the temporal and spectral analyses of the gamma-ray emission over wide energy ranges. Sufficiently detailed information cannot be determined from the gamma-ray observations alone and coincident observations of solar energetic particles (SEP) in interplanetary space and high-energy neutron measurements at ground-based stations are required to complement the data.

The Wide Band Spectrometer (WBS), which consists of three kinds of spectrometers covering the energy range from soft X-rays to gamma-rays, is installed on the SOLAR-A to observe the detailed spectrum and temporal evolution of this wide-band photon emission. It will help to better understand the important processes of plasma heating and particle acceleration in solar flares.

2. Instrument Description

The WBS consists of the following subinstruments: (1) soft X-ray spectrometer (SXS), (2) hard X-ray spectrometer (HXS), (3) gamma-ray spectrometer (GRS), and (4) radiation belt monitor (RBM). SXS, HXS, and GRS are solar instruments pointed at the Sun. RBM has the capability of detecting the radiation belt passage and is pointed perpendicular to the solar direction. Descriptions of the WBS instrument can be found elsewhere (Yoshimori, 1988; Yoshimori *et al.*, 1988; Kondo *et al.*, 1990).

2.1. Soft X-ray spectrometer (SXS)

SXS consists of a gas proportional counter filled with Xe and CO_2 (1.16 atm) and covers the energy range of 2 to 30 keV. The gas proportional counter has three anode wires: two of them are connected together to form SXS-1 output and the third anode wire forms SXS-2 output. The cross-sectional view of the SXS detector is shown in Figure 1. The three anode wires are biased with one high-voltage power supply unit. SXS has a field of view of 10 deg × 10 deg (20 times the diameter of the Sun), reducing the background by an aluminum slit collimator. The SXS counters have beryllium windows of 150 μm thickness. The SXS-1 counter has an area of 11.88 cm^2 with the additional 150 μm thick aluminum filter and 0.0707 cm^2 without filters, while the SXS-2 counter has aluminum filters of 50 μm thickness (0.0353 cm^2) and 300 μm thickness (6.12 cm^2). The effective areas of SXS-1 and SXS-2 counters are calculated as a function of energy and shown in Figure 2. The SXS-1 counter has a large effective area suitable for detection of a small flare, whereas the SXS-2 counter has a small effective area suitable for detection of large flares. Thus the SXS, with the two different gas proportional counters, has the capability of detecting flares of various sizes.

The SXS spectral response to a 5.9 keV Mn Kα line from the ^{55}Fe radioactive source is shown in Figure 3. The energy resolution (FWHM) at 5.9 keV is about 20% and is shown as a function of energy in Figure 4. The in-flight energy calibration is achieved by detection of the 5.9 keV Mn Kα line of the attached ^{55}Fe calibration source.

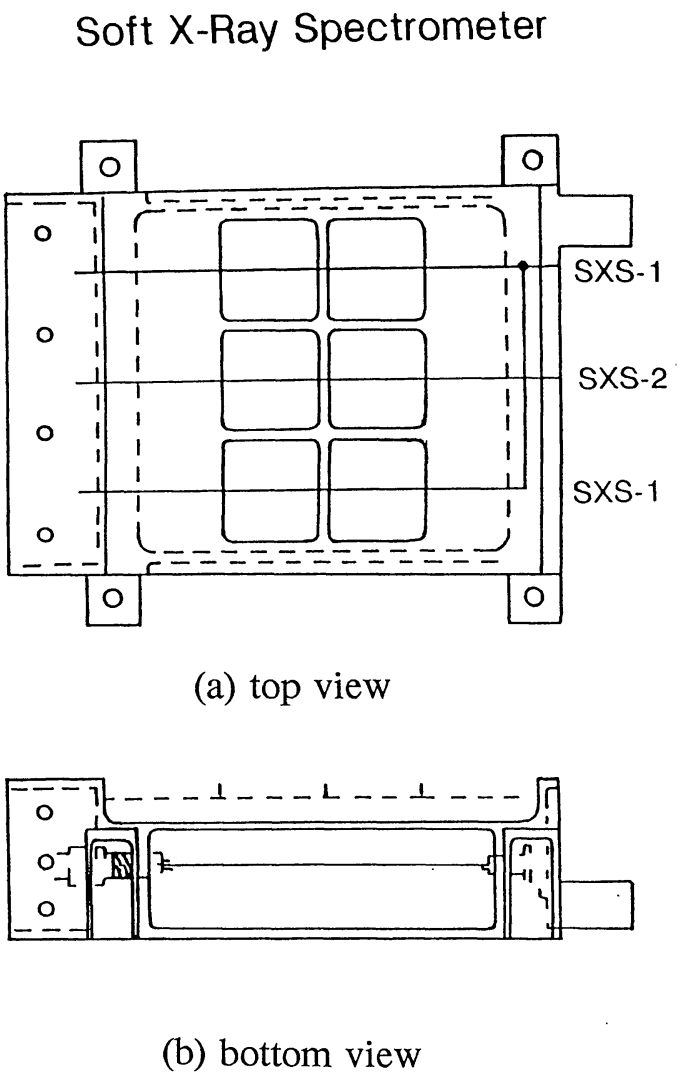

Fig. 1. Cross-sectional view of SXS gas proportional counter. (a) Top view and (b) side view. The SXS gas proportional counter has three anode wires: two of them are connected together to form SXS-1 output and the third wire forms SXS-2 output.

The SXS electronic block diagram is shown in Figure 5. The SXS primary output data from both SXS-1 and SXS-2 counters are 128-channel pulse height data in the 2–30 keV range every 2 s (SXS-PH1 for SXS-1 and SXS-PH2 for SXS-2) and 2-channel pulse count data every 0.25 s (SXS-PC11 and 12 for SXS-1 and SXS-PC21 and 22 for SXS-2). The energy ranges of the pulse count data are changeable by command. One of the 4 pulse count data is also used to monitor the occurrence of solar flares.

2.2. Hard X-ray spectrometer (HXS)

The HXS consists of a NaI scintillator, which is 7.6 cm in diameter and 2.5 cm in thickness, optically coupled to a 7.6 cm diameter photomultiplier tube. The cross-sectional view of the HXS is shown in Figure 6. The HXS covers the energy range of

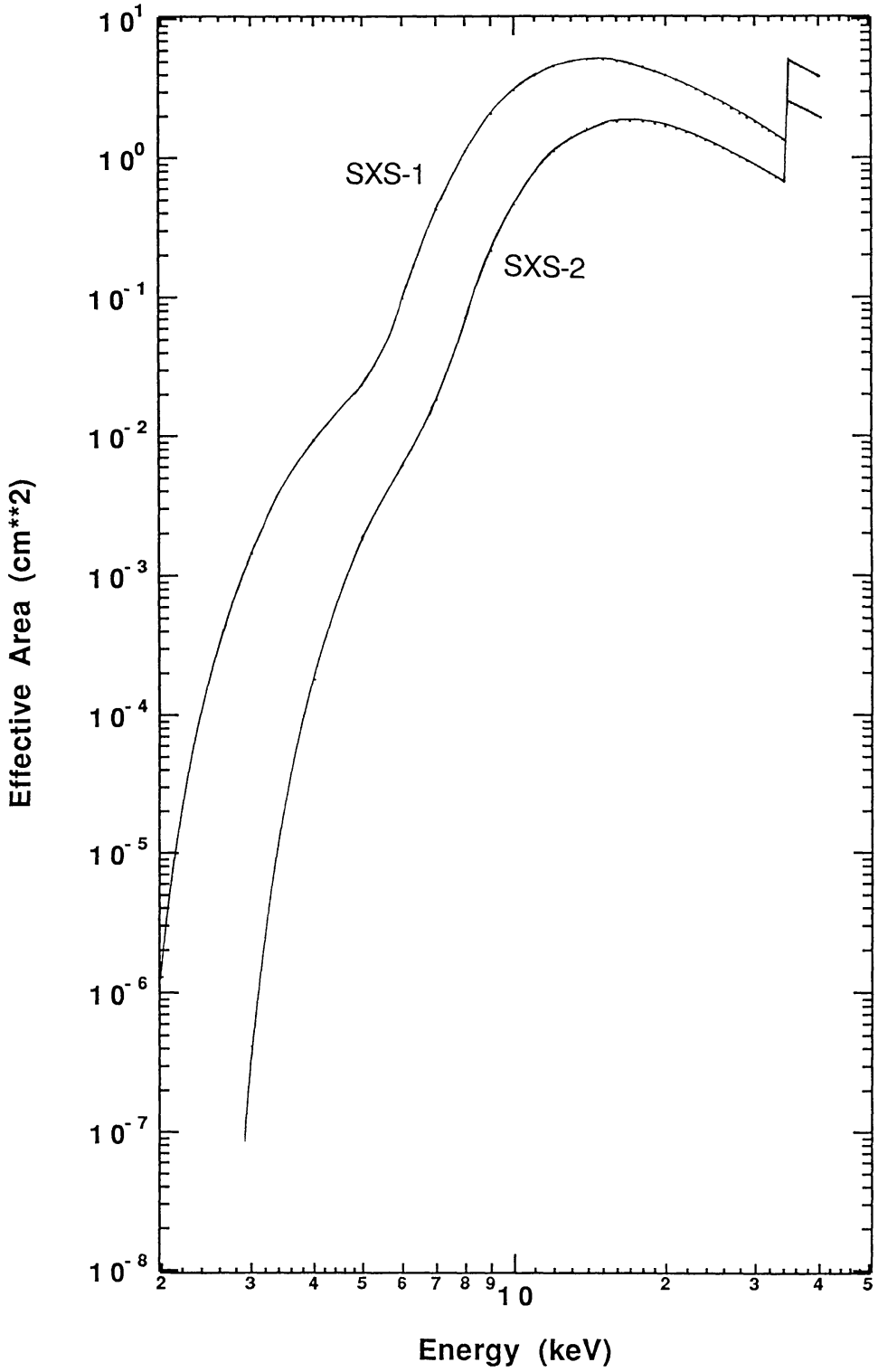

Fig. 2. Calculated effective areas of SXS-1 and SXS-2 counters as functions of X-ray energy.

20–600 keV. The NaI scintillator is covered with two stainless steel absorbers (13.8 cm^2 × 0.08 mm thick + 31.8 cm^2 × 1 mm thick) to suppress low-energy X-ray events. The effective area of HXS is shown as a function of energy in Figure 7. The HXS spectral response to 30, 81, and 356 keV lines from ^{133}Ba electron capture is shown in

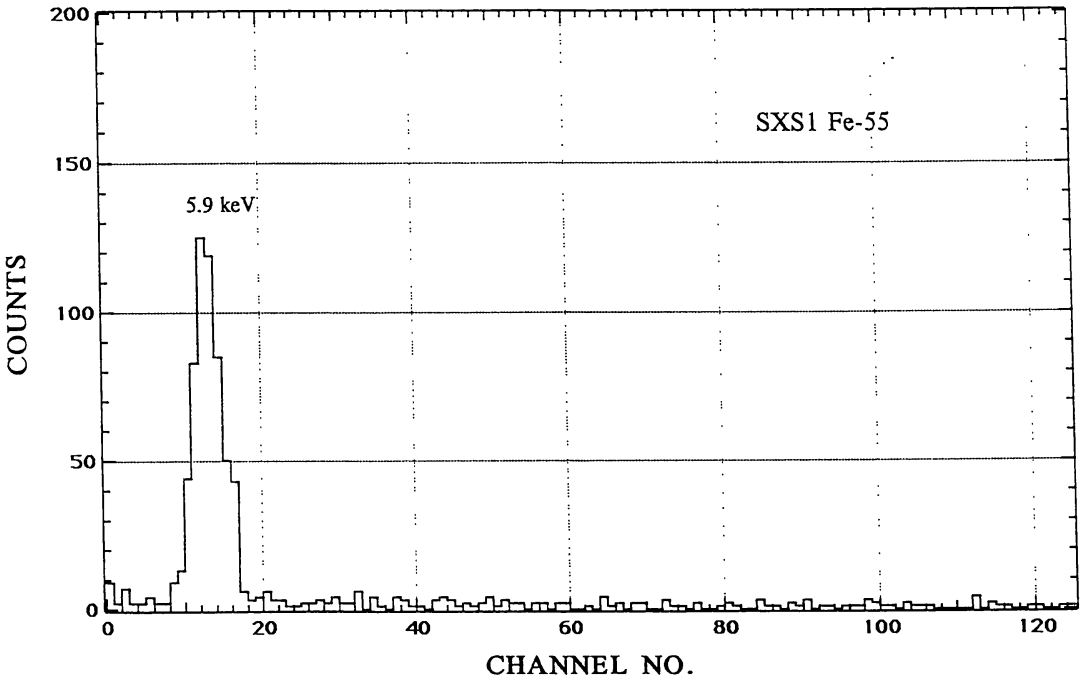

Fig. 3. SXS spectral response to 5.9 keV Mn Kα line from ^{55}Fe radioactive source.

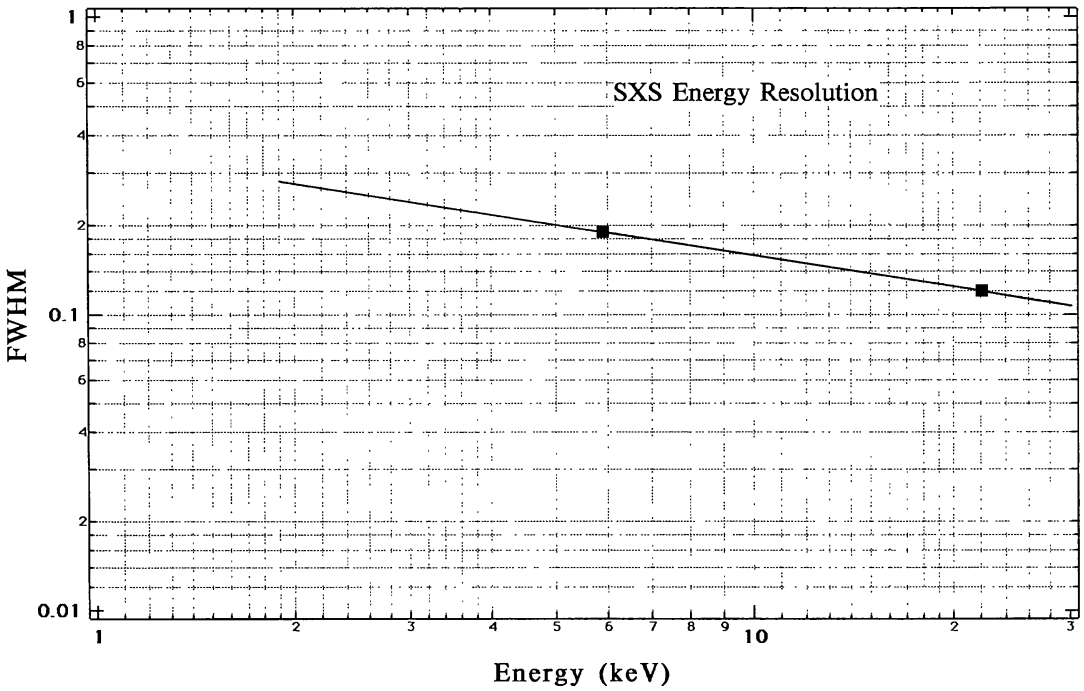

Fig. 4. Energy resolution (FWHM) of the SXS counter as function of energy.

Figure 8. The energy resolution (FWHM) at 60 keV is 15% and is shown as a function of energy in Figure 9. The incident hard X-ray spectrum is obtained by deconvoluting the observed 32-channel energy-loss spectrum (Forrest, 1990). An HXS response matrix obtained from the Monte Carlo simulation is used for the spectral deconvolution. As an example, the incident hard X-ray spectrum of E^{-3} below 100 keV and E^{-5} above

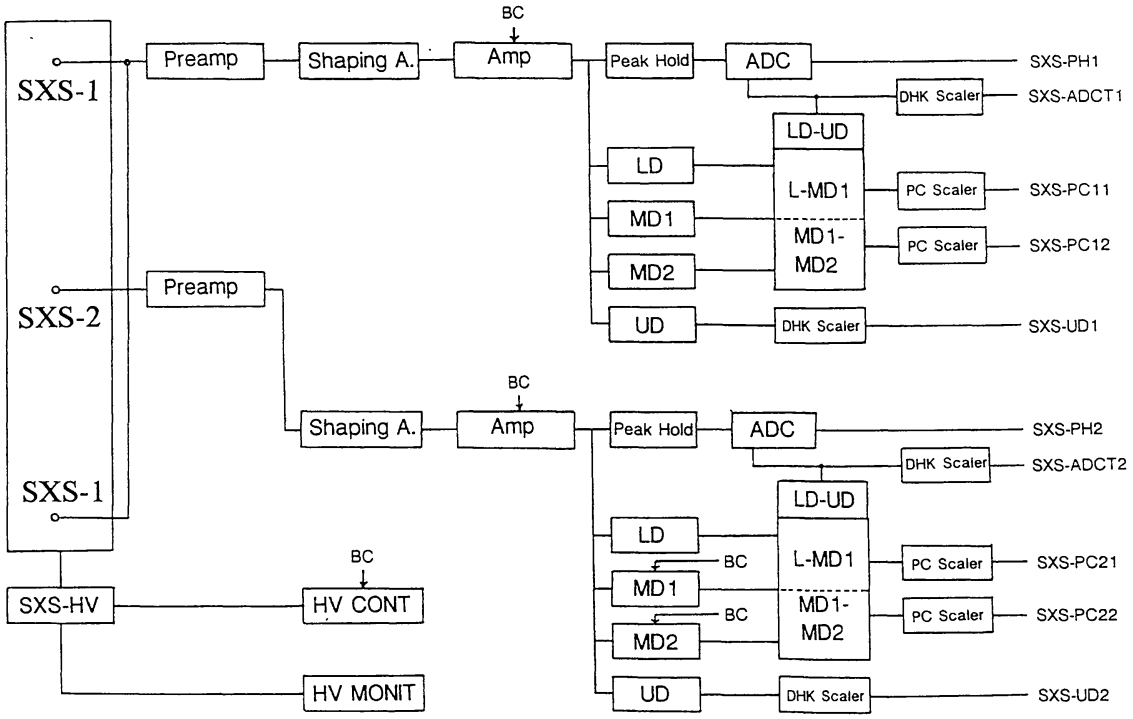

Fig. 5. SXS electronic block diagram. Three anode wires are biased by one high-voltage power supply unit (HV). Each of the SXS-1 and SXS-2 outputs is fed to a similar electronic circuit. Each of the SXS counter outputs passes through a preamplifier and shaping amplifier, and is fed to a main amplifier. After amplification, the output is sent to an 8-bit ADC to produce 128-channel pulse height data (SXS-PH). The amplified output is also sent to a discriminator with 4 levels (LD, MD1, MD2, and UD) to produce 2-channel pulse height count data (SXS-PC11 and 12 for SXS-1 and SXS-PC21 and 22 for SXS-2). In addition, ADC triggering count (SXS-ADCT), and pulse count above upper discriminator level (SXS-UD) are monitored as housekeeping data. HV level, main amplifier gain, and MD1 and MD2 discrimination levels are changeable by block command (BC).

100 keV and the convoluted energy-loss spectrum are shown in Figure 10. The in-flight energy calibration is achieved by detection of a 60 keV line from ^{237}Np nuclear de-excitation (^{237}Np is an ^{241}Am α-decay product). In this HXS calibration, the 60 keV line event in coincidence with an α-particle (5.48 MeV) event detected with two silicon detectors is recorded. The in-flight energy calibration method is schematically shown in Figure 11. The HXS in-flight energy calibration spectrum measured with the coincidence method is shown in Figure 12. The details of the in-flight energy calibration system was described earlier (Yoshimori and Okudaira, 1988).

The HXS electronic block diagram is shown in Figure 13. The HXS primary output is 32-channel quadratic-spaced pulse height data in the 20–400 keV range every 1 s (HXS-PH), and 2-channel pulse count data (HXS-PC1 (20–50 keV) and HXS-PC2 (50–600 keV)) every 0.125 s. HXS-PC1 is also used to monitor the occurrence of solar flares.

2.3. Gamma-ray spectrometer (GRS)

The GRS consists of two identical BGO scintillators. Each scintillator is 7.6 cm in diameter and 5.1 cm in thickness and is optically coupled to a 7.6 cm diameter photo-

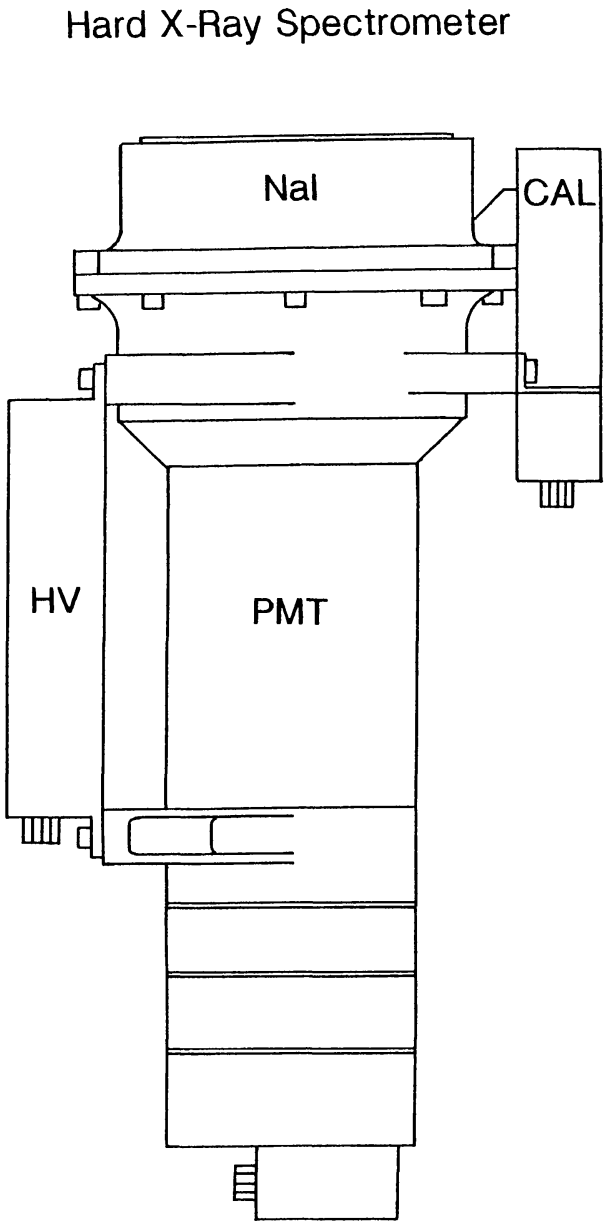

Fig. 6. Cross-sectional view of HXS NaI detector. A NaI(T1) scintillator of 7.6 cm diameter and 2.5 cm thickness is optically coupled with a photomultiplier tube (PMT) biased by a high-voltage power supply unit (HV). CAL is an in-flight energy calibration device.

multiplier tube. The cross-sectional view of GRS is shown in Figure 14. Since the BGO ($Bi_4Ge_3O_{12}$) scintillator has high density and high effective atomic number, these properties contribute toward improving the detection sensitivity to gamma-rays. Each BGO scintillator is covered with a 0.5 mm thick lead absorber to suppress low-energy gamma-ray events. The GRS spectral responses to 3.08 and 4.07 MeV lines from ^{49}Ca nuclear de-excitation (^{49}Ca nuclear excitation state is produced by thermal neutron-capture reaction of ^{48}Ca nuclei) and 12.79 and 17.23 MeV lines from ^{7}Be nuclear de-excitation (^{7}Be nuclear excited state is produced by nuclear reaction of $p(^{7}\text{Li}, ^{7}\text{Be})n$)

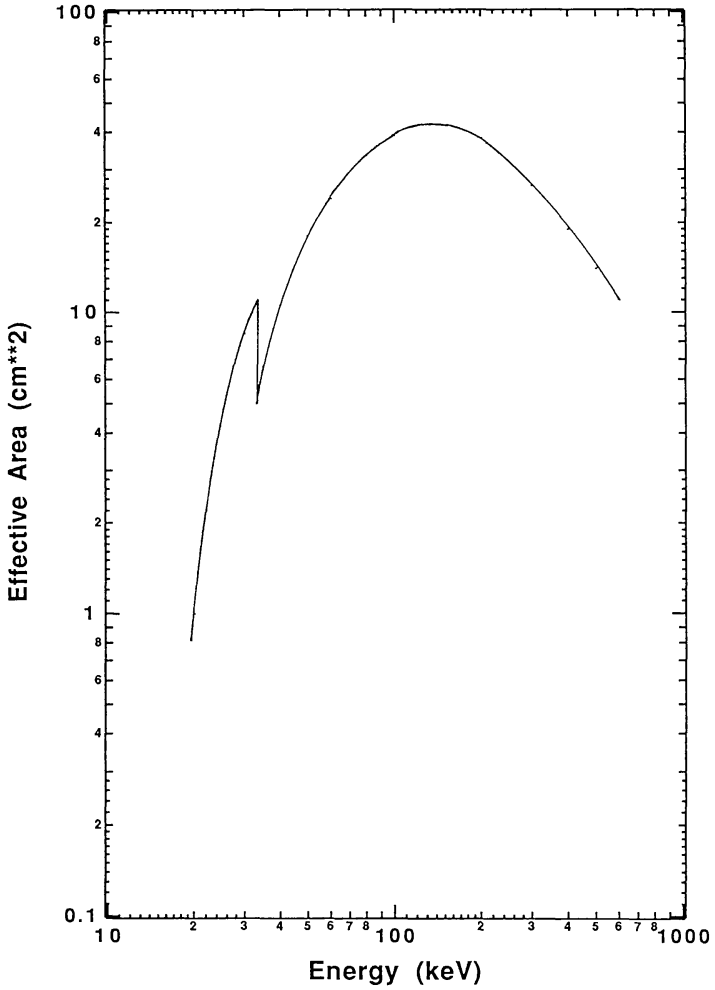

Fig. 7. Calculated effective area of HXS as a function of X-ray energy.

are shown in Figures 15(a) and 15(b). The energy resolution (FWHM) of GRS is shown as a function of energy in Figure 16. The BGO energy resolution is about twice that of the NaI scintillator due to the low scintillation efficiency of the BGO scintillator. The energy dependence of the effective area of GRS is calculated as a function of gamma-ray energy by the Monte-Carlo simulation. The result is shown in Figure 17. The incident gamma-ray spectrum is obtained by deconvoluting the observed 128-channel energy-loss spectrum. The GRS response matrix obtained from the Monte Carlo simulation is used for the spectral deconvolution. As an example, the incident gamma-ray spectrum of E^{-3} continuum + lines and the convoluted energy-loss spectrum are shown in Figure 18.

The GRS electronic block diagram is shown in Figure 19. Each of two identical GRS detectors (GRS-1 and GRS-2) is connected to a similar electronic circuit. Since GRS covers the wide energy range of 0.2–100 MeV, the 0.2–10 MeV output pulse (GRS-L) and 8–100 MeV output pulse (GRS-H) are produced from the anode and the 6th dynode of the photomultiplier tube, respectively. The primary output data of GRS-L are 128-channel quadratic-spaced pulse height data every 4 s (GRS-PHL1 and

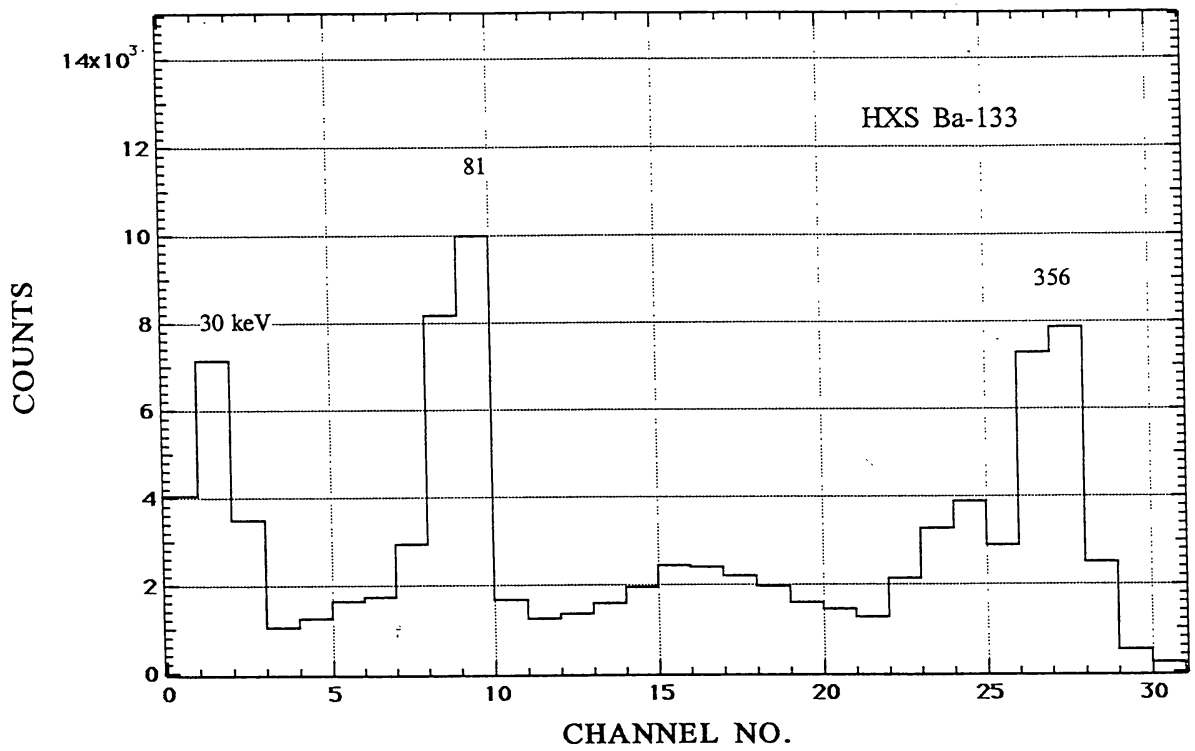

Fig. 8. HXS spectral response to 30, 81, and 356 keV lines from ^{133}Ba electron capture.

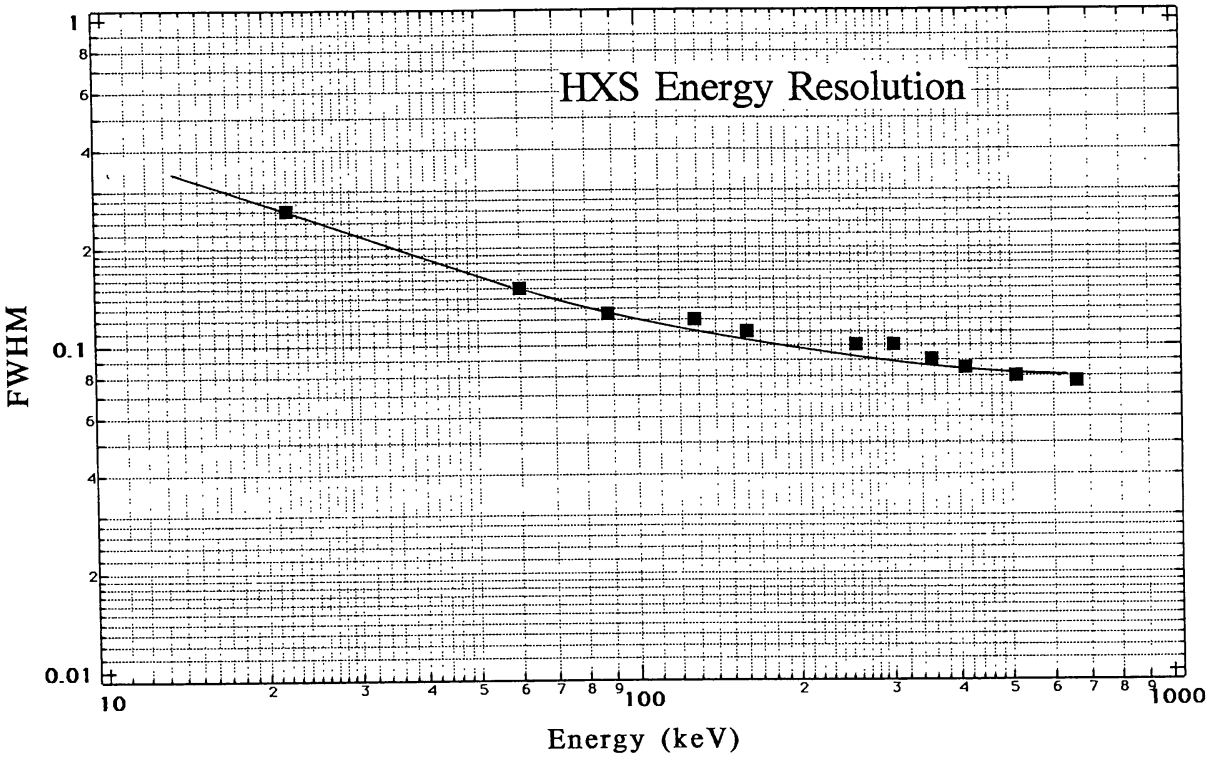

Fig. 9. Energy resolution (FWHM) of HXS as a function of energy.

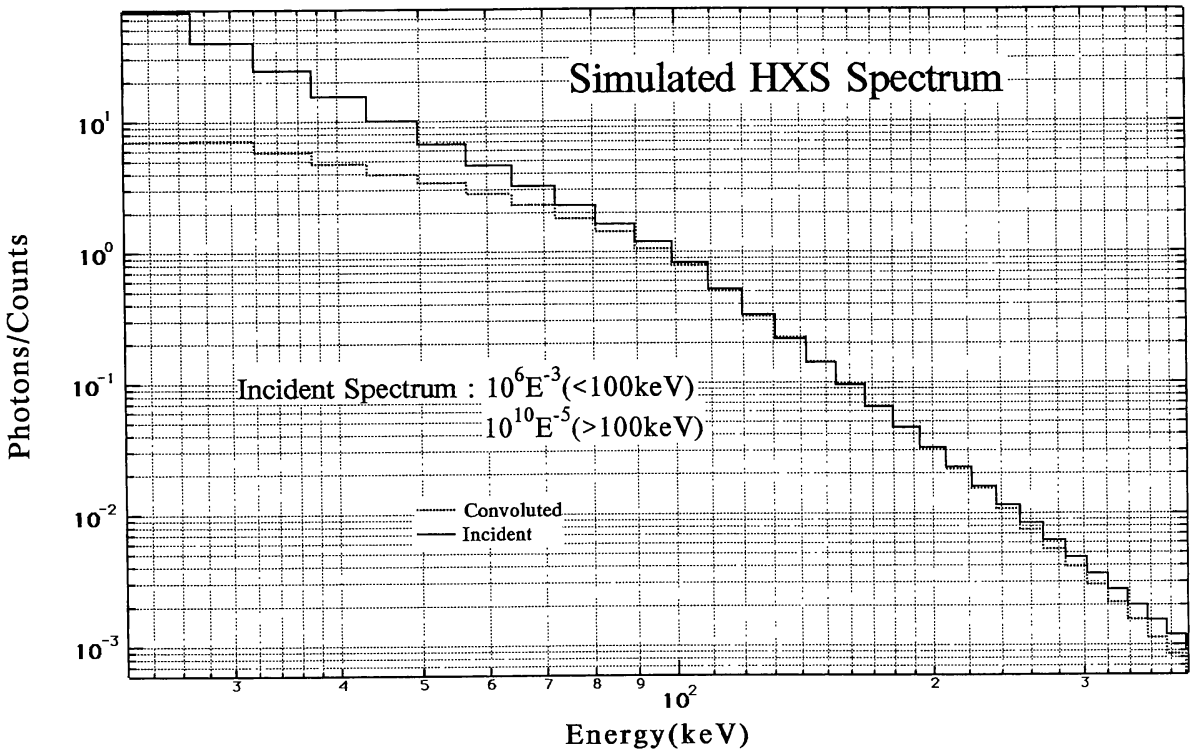

Fig. 10. Hard X-ray incident spectrum (E^{-3} below 100 keV and E^{-5} above 100 keV) and convoluted energy-loss spectrum.

GRS-PHL2) and 4-channel pulse count data (GRS-PC11 and 21 for 0.2–0.7 MeV, GRS-PC12 and 22 for 0.7–4 MeV, GRS-PC13 and 23 for 4–7 MeV and GRS-PC14 and 24 for 7–10 MeV). The time resolution is 0.25 s for GRS-PC11, 12, 21, and 22, and 0.5 s for GRS-PC13, 14, 24, and 25. The primary output data of GRS-H are 16-channel

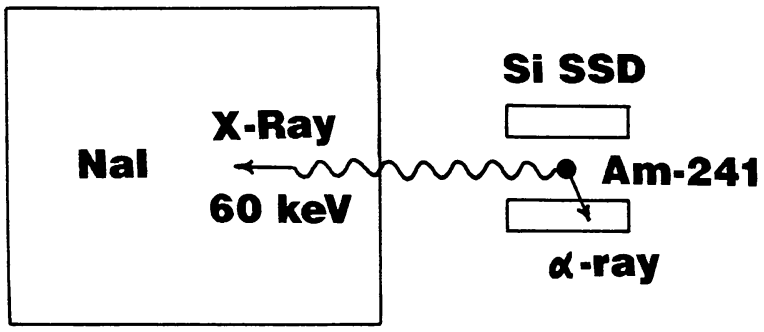

Fig. 11. HXS in-flight energy calibration method is schematically shown. 60 keV nuclear de-excitation line and 5.48 MeV α-ray are simultaneously emitted from ^{241}Am radioactive source. 60 keV line detected with HXS NaI(T1) scintillator in coincidence with 5.48 MeV α-ray detected with two silicon solid state detetors (Si SSD) is recorded as calibration data.

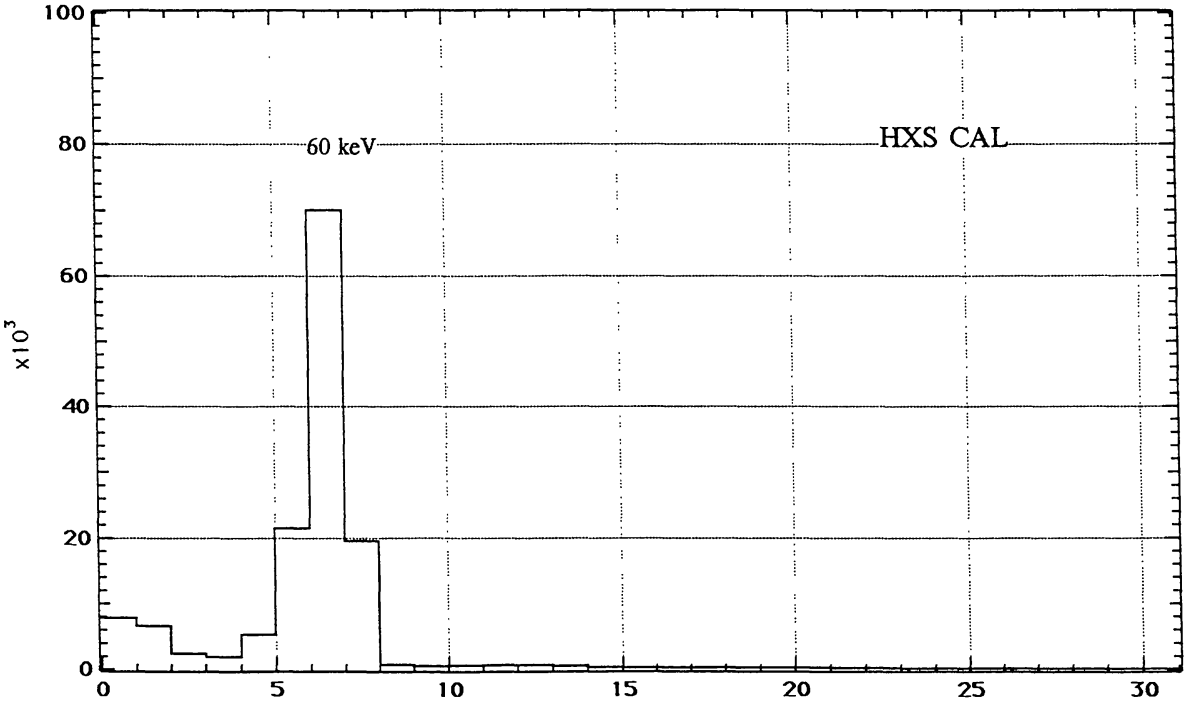

Fig. 12. HXS in-flight energy clibration spectrum of 60 keV line from ^{237}Np nuclear de-excitation.

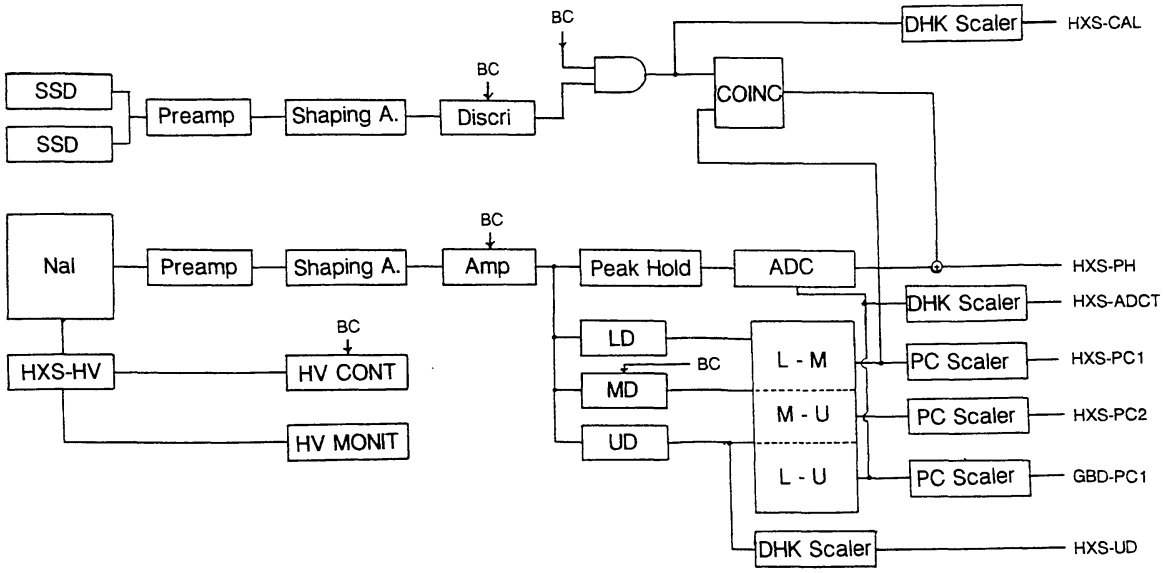

Fig. 13. HXS electronic block diagram. NaI(T1) scintillation detector output passes through a pre-amplifier and shaping amplifier, and is fed to a main amplifier. After amplification, the output is sent to an 8-bit ADC to produce 32-channel pulse height data (HXS-PH). The amplified output is also sent to a discriminator with 3 levels (LD, MD, and UD) to produce 2-channel pulse count data (HXS-PC1 and HXS-PC2). Silicon solid state detector (SSD) output passes through a preamplifier and shaping amplifier, and is fed to a discriminator. A coincidence event between NaI(T1) and SSD detectors provides an in-flight energy calibration event. In addition, ADC triggering count (HXS-ADCT), pulse count above upper discrimination level (HXS-UD), and SSD pulse count (HXS-SSD) are monitored as house-keeping data. HV level, main amplifier gain, SSD discrimination level, and NaI(T1) discrimination level are changeable by block command (BC).

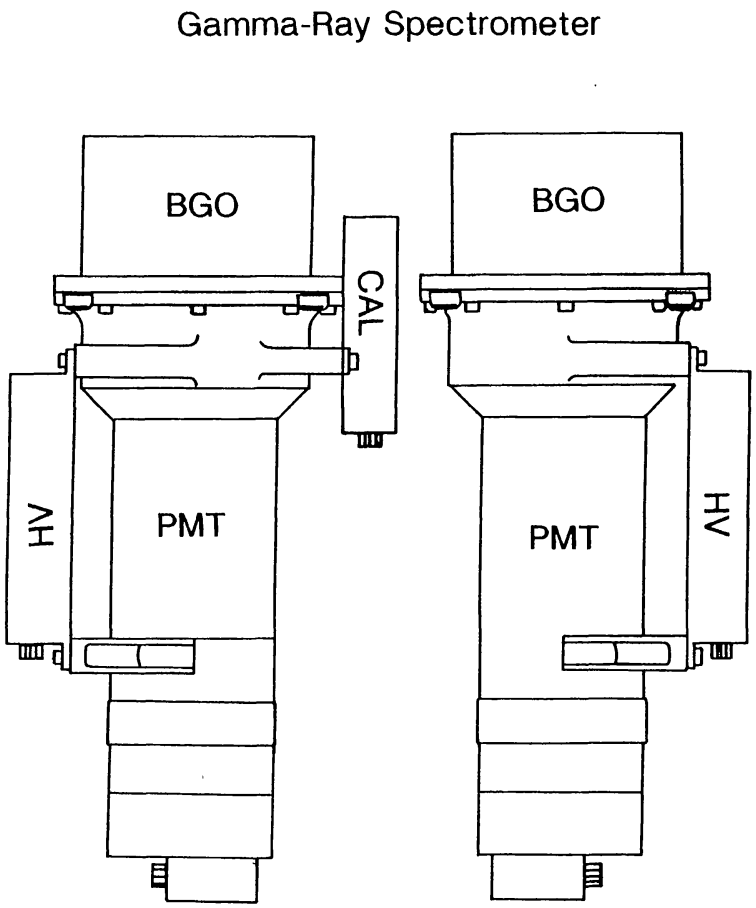

Fig. 14. Cross-sectional view of GRS. GRS consists of two identical BGO ($Bi_4Ge_3O_{12}$) scintillators (7.6 cm diameter and 5.0 cm thickness) optically coupled to photomultiplier tube (PMT). Each PMT is biased by high-voltage power supply unit (HV). CAL is an in-flight energy calibration device used for two BGO detectors.

pulse height data every 4 s (GRS-PHH1 and GRS-PHH2) and 2-channel pulse count data every 0.5 s (GRS-PC15 and 25 for 8–30 MeV and GRS-PC16 and 26 for 30–100 MeV). The in-flight energy calibration in GRS-L is achieved by the detection of 1.17 and 1.33 MeV lines from ^{60}Co nuclear de-excitation in coincidence with a β-ray (maximum energy 310 keV) detected with two Si detectors. The GRS in-flight energy calibration spectrum measured with the coincidence method is shown in Figure 20.

GRS also has detection sensitivity to solar neutrons. As an example, the GRS response to 45 MeV neutrons produced by p(Li, Be)n reaction is shown in Figure 21. Although the GRS has sensitivity to neutrons, it is difficult to determine the incident neutron energy from the GRS pulse height spectrum.

2.4. Radiation Belt Monitor (RBM)

The RBM consists of two different detectors, NaI scintillation detector (5.1 cm in diameter and 1 cm in thickness) and Si detector (4 mm in diameter and 100 μm in thickness). These two detectors are pointed in the direction perpendicular to the Sun and are insensitive to solar flare X-rays and gamma-rays. The NaI detector produces

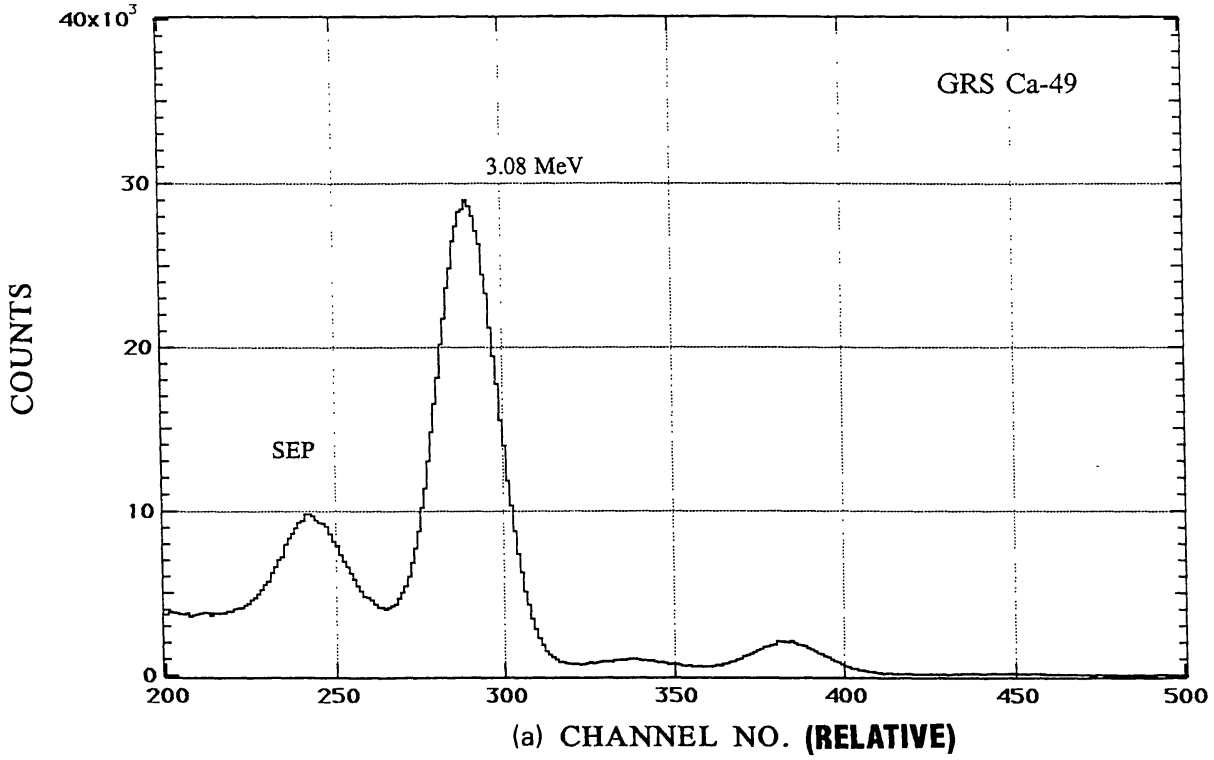

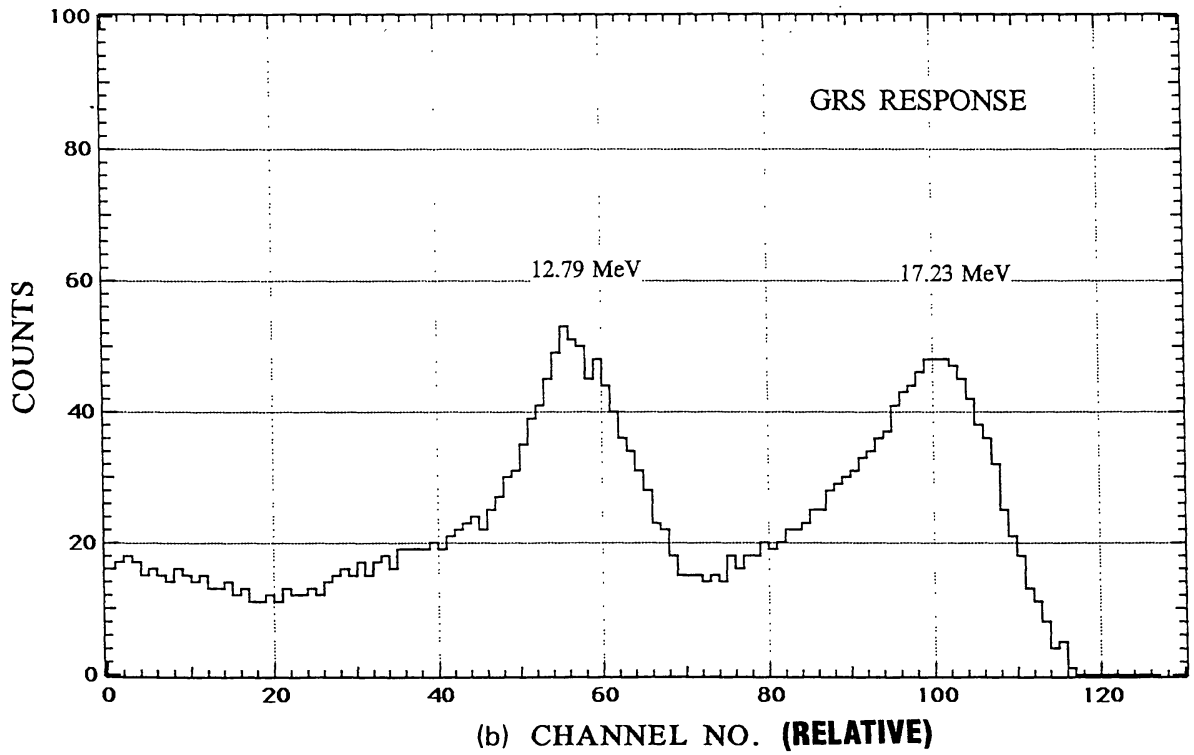

Fig. 15. (a) GRS spectral response to 3.08 and 4.07 MeV lines from ^{49}Ca nuclear de-excitation. (b) GRS spectral response to 12.79 and 17.23 MeV lines from ^{7}Be nuclear de-excitation.

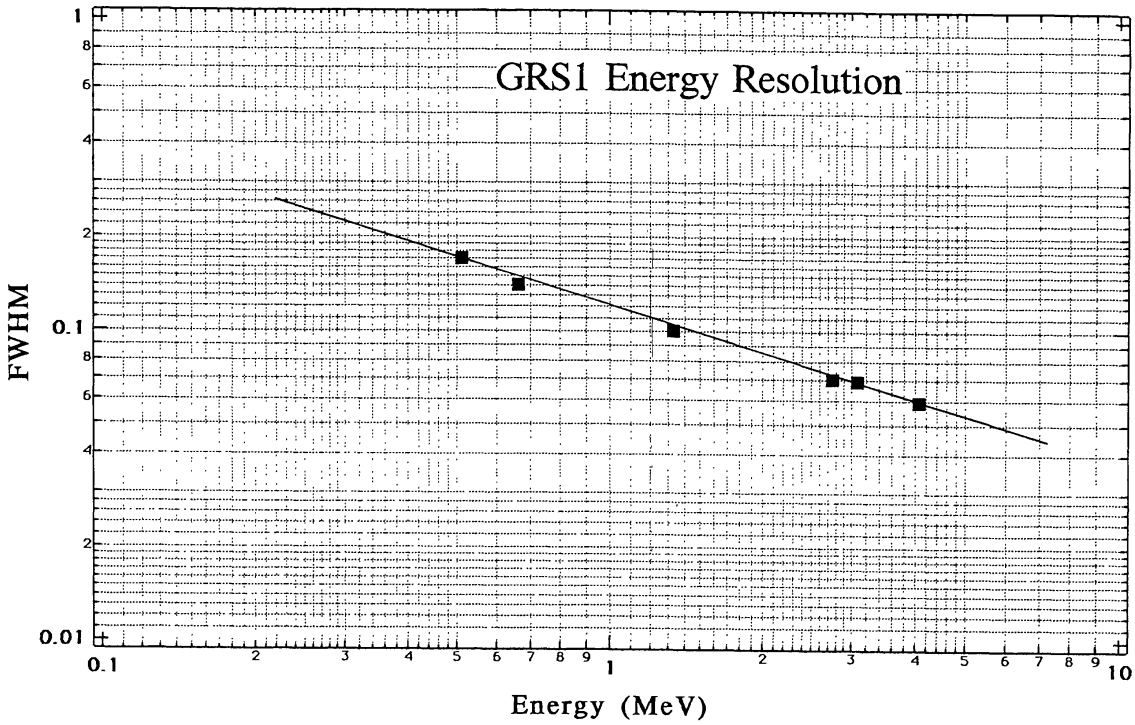

Fig. 16. Energy resolution (FWHM) of GRS as a function of energy.

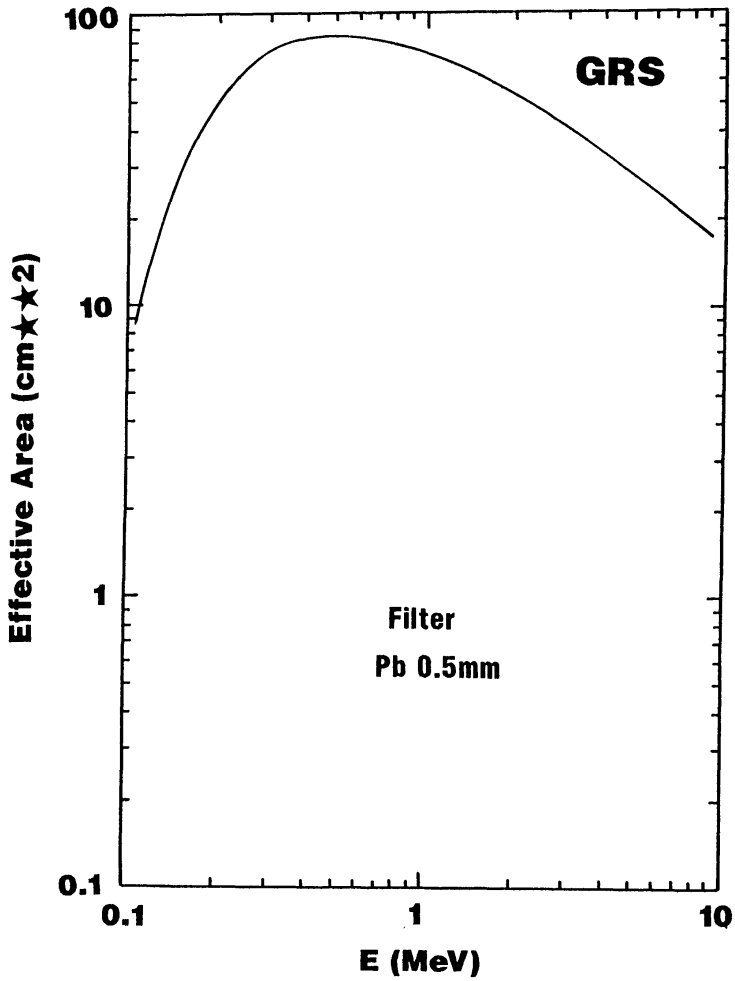

Fig. 17. Calculated effective area of GRS as a function of energy.

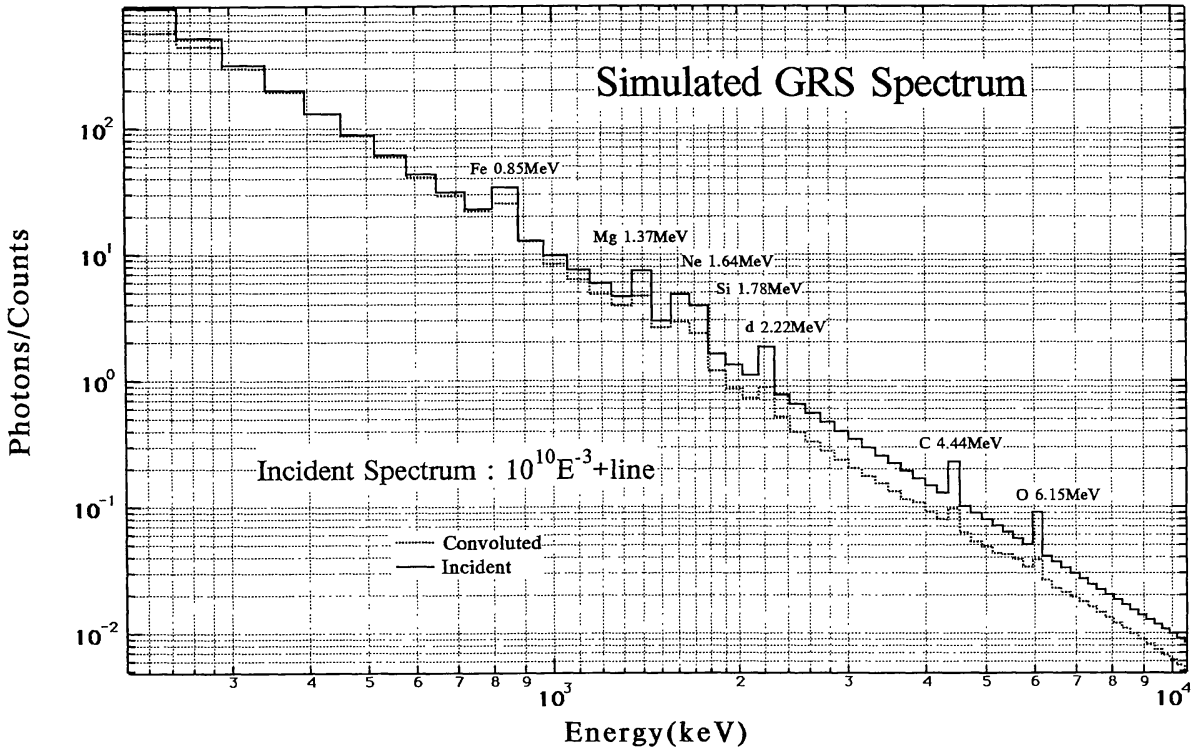

Fig. 18. Gamma-ray incident spectrum (E^{-3} + lines) and convoluted energy-loss spectrum.

32-channel quadratic-spaced pulse height data in the 5–300 keV range every 1 s and 2-channel pulse count data (5–60, 60–300 keV) every 0.25 s. The Si detector produces single channel pulse count data in energies above 20 keV every 0.25 s. When the pulse count of the NaI or the Si detector exceeds a certain threshold value, the alarm for the South Atlantic Anomaly (SAA) passage is sounded. The radiation belt alarm is used to avoid recording a false flare event.

2.5. Gamma-ray burst detection capability

The HXS and RMB NaI detectors are capable of monitoring non-solar X-ray and gamma-ray burst phenomena during solar quiet time and night time. When the HXS

Fig. 19. GRS electronic block diagram. GRS consists of two identical BGO ($Bi_4Ge_3O_{12}$) scintillation detectors (GRS-1 and GRS-2). Each detector is connected to a similar electronic circuit and produces two outputs. One is an anode output pulse (0.2–10 MeV) and the other is a 6th dynode output pulse (8–100 MeV). The anode pulse passes through a preamplifier and shaping amplifier, and is fed to a main amplifier. After amplification, the output pulse is sent to an 8-bit ADC to produce 128-channel pulse height data (GRS-PHL). The amplified pulse is also sent to a discriminator with 5 levels to produce 4-channel pulse count data (GRS-PC11, 12, 13, and 14 for GRS-1 and GRS-PC21, 22, 23, and 24 for GRS-2). The dynode pulse is similarly processed to produce 16-channel pulse height data (GRS-PH) and 2-channel pulse count data (GRS-PC25 and 26 for GRS-2). Two silicon solid state detectors (SSD) output is fed to a preamplifier and shaping amplifier, and then sent to a discriminator. A coincidence event between the BGO and SSD detectors provides an in-flight energy calibration event. In addition, ADC triggering event (GRS-ADCLT and GRS-ADCHT), pulse count above upper discrimination level (GRS-UD), and SSD pulse count (GRS-CAL) are monitored as housekeeping data. HV level, main amplifier gain, and SSD discrimination level are changeable by block command (BC).

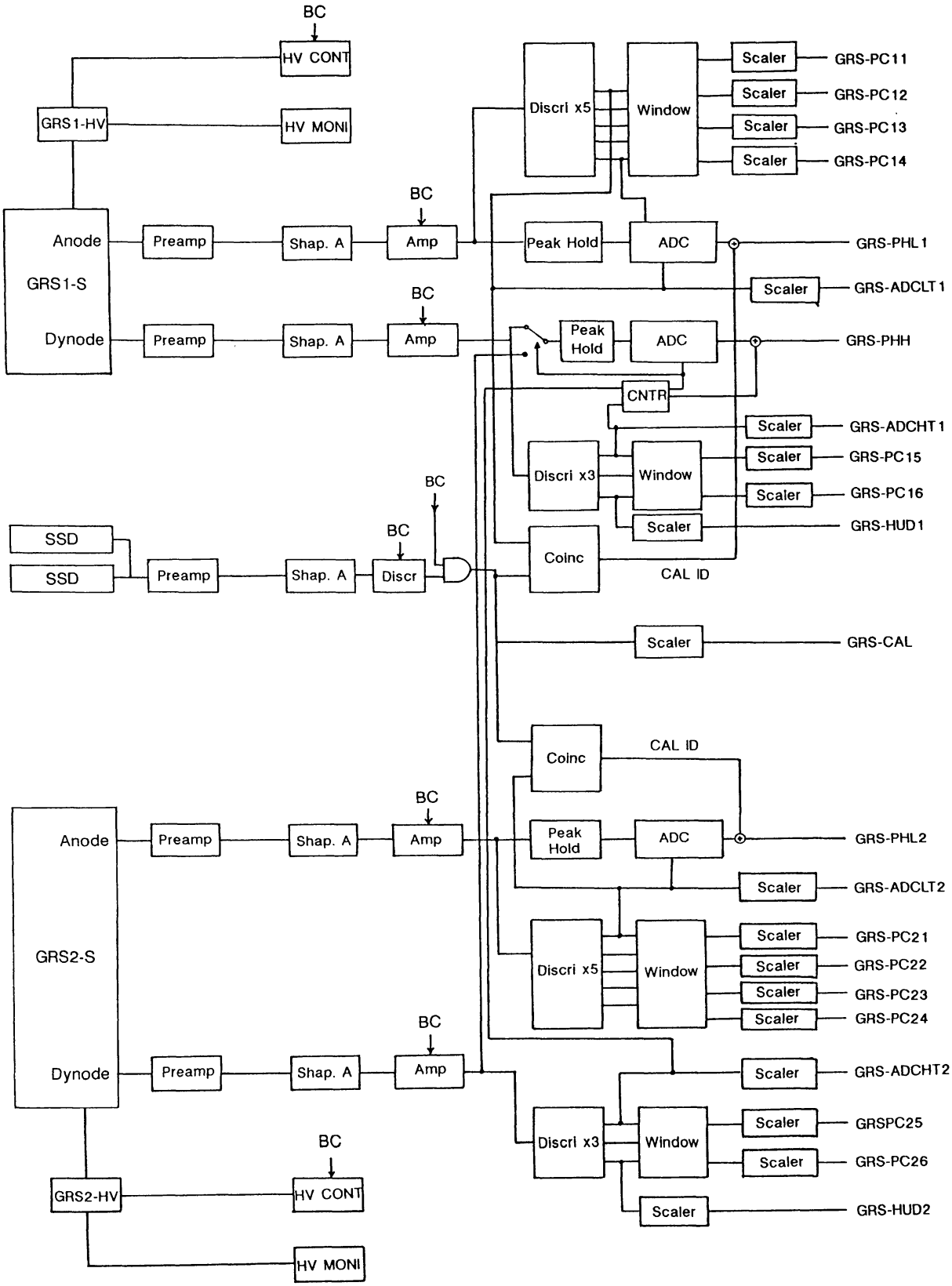

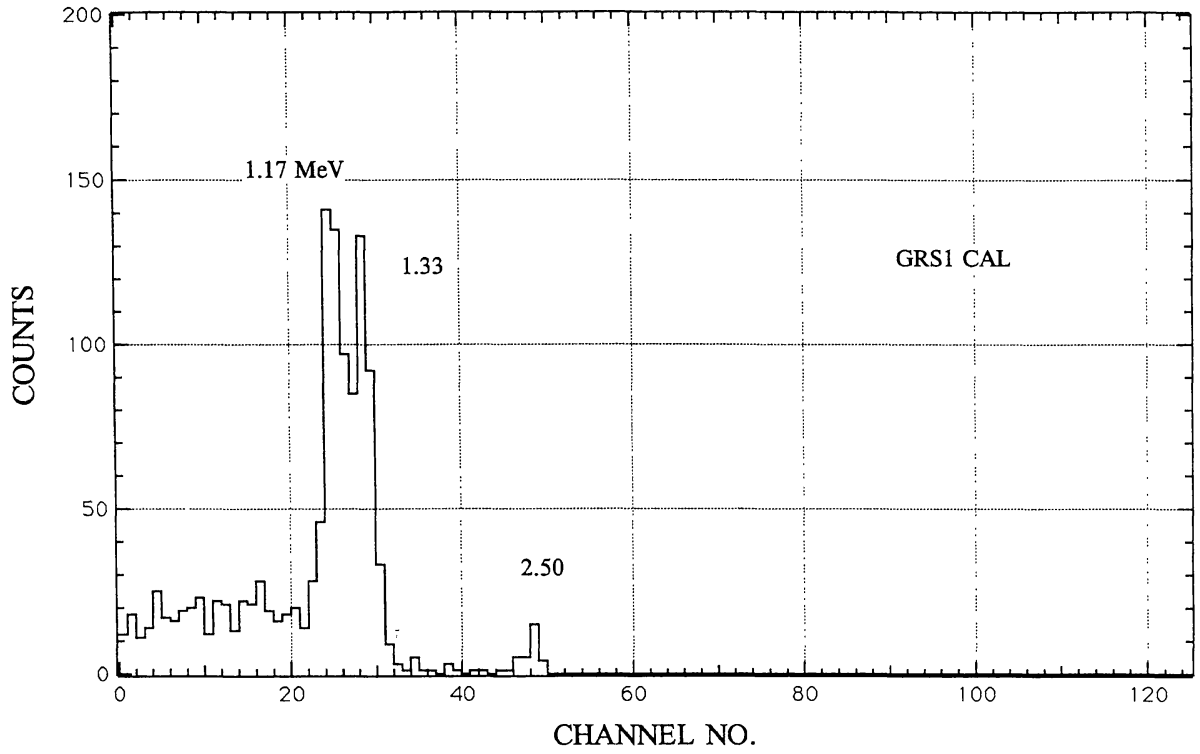

Fig. 20. GRS in-flight energy calibration spectrum of 1.17 and 1.33 MeV lines from ^{60}Co nuclear de-excitation.

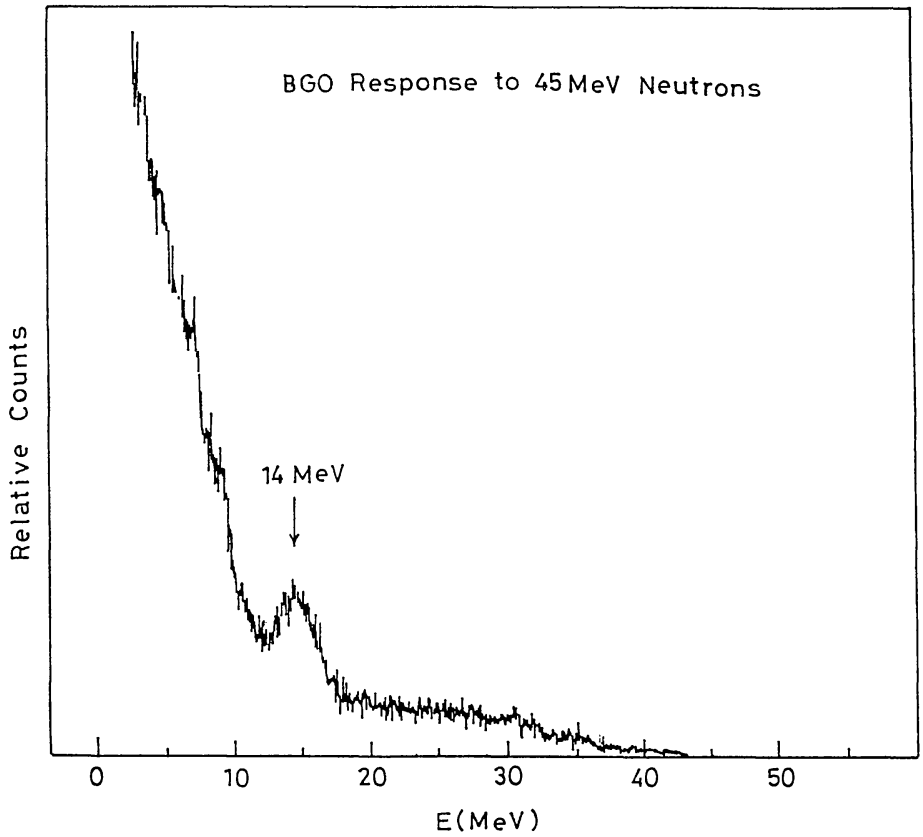

Fig. 21. GRS response to 45 MeV neutrons.

pulse count in the 50–600 keV range or the RBM pulse count in the 60–300 keV range exceeds a certain threshold value, both 32-channel pulse height data every 1 s and pulse count data every 0.25 s are recorded for 256 s.

TABLE I

Principal WBS output data. SXS consists of two different gas proportional counters (SXS-1 and SXS-2) and each counter provides 128-channel pulse height (PH) data every 2 s, and 2-channel pulse count (PC) data every 0.25 s. HXS consists of a NaI scintillation detector and provides 32-channel PH data every 1 s, and 2-channel PC data every 0.125 s. GRS consists of two identical BGO scintillation detectors (GRS-1 and GRS-2) and each detector provides 128-channel (0.2–10 MeV) and 16-channel (8–100 MeV) PH data every 4 s, and 6-channel PC data every 0.25 or 0.5 s.

Spectrometer	Output	PH-data (time resolution)	PC-data (time resolution)
SXS	SXS-1	128-ch (2–30 keV) (2 s)	2-ch (0.25 s)
	SXS-2	128-ch (2–30 keV) (2 s)	2-ch (0.25 s)
HXS	HXS	32-ch (20–600 keV) (1 s)	2-ch (0.125 s)
GRS	GRS-1	128-ch (0.2–10 MeV) (4 s)	4-ch (0.25 s)
		16-ch (8–100 MeV) (4 s)	2-ch (0.5 s)
	GRS-2	128-ch (0.2–10 MeV) (4 s)	4-ch (0.25 s)
		16-ch (8–100 MeV) (4 s)	2-ch (0.5 s)

The principal WBS data are given in Table I. In addition to the principal data, housekeeping data are also recorded. These data include command status, instrument status, sixteen digital housekeeping data (the counts above upper energy discrimination level, ADC triggering counts, and inflight energy calibration event counts) and nine analog housekeeping data (high voltage and temperature).

3. Expected Scientific Return

WBS is expected to produce the following results. From the SXS observation the time development of electron temperatures and emission measures of a heated plasma can be studied and the cutoff energy of the nonthermal electron spectrum will be determined. The SXS observations can contribute to solving some fundamental problems of plasma heating during solar flares. From the HXS and GRS observations the electron and ion acceleration processes can be characterized in greater detail and the physical conditions which dominate the time scale and the efficiency of the particle acceleration mechanisms can be better determined. The WBS observations will provide an essential key to our understanding of high-energy processes such as plasma heating, particle acceleration, and interaction processes during solar flares.

Furthermore, collaborations with the other instruments of SOLAR-A (soft X-ray telescope, hard X-ray telescope, and Bragg crystal spectrometer), gamma-ray instruments on GRO and GRANAT, Max '91 HIREGS (high-resolution gamma-ray spectrometer) and HEIDI (high-energy imaging device), radio imagers at microwave and

millimeter wavelengths, solar energetic particle (SEP) instruments on GEOTAIL and WIND, and ground-based solar neutron monitors will provide very fruitful and exciting results which may help us to solve a lot of questions related to the high-energy solar flare phenomena.

Acknowledgement

The authors wish to thank Toshiba Corporation for the detailed design, fabrication and testing of the electronics and for the integration of the WBS system.

Note Added in Proof

The HXS in-flight energy calibration method described here is not adopted. The HXS in-flight energy calibration is achieved by detection of 60 keV line of the attached Am-241 calibration source.

References

Chupp, E. L.: 1984, *Ann. Rev. Astron. Astrophys.* **22**, 359.
Chupp, E. L.: 1987, *Phys. Scripta* **T18**, 5.
Dennis, B. R.: 1988, *Solar Phys.* **118**, 49.
Forrest, D. J.: 1990, *21st Int. Cosmic Ray Conf.* **7**, 241.
Kondo, I., Yoshimori, M., Okudaira, K., Hirasima, Y., Igarashi, T., Akasaka, M., Nishimura, J., Yamagami, T., Ohki, K., and Watanabe, T.: 1990, *21st Int. Cosmic Ray Conf.* **7**, 268.
Watanabe, T., Tanaka, K., Akita, K., and Nitta, N.: 1983, *Solar Phys.* **83**, 107.
Yoshimori, M.: 1988, in N. Gehrels and G. H. Share (eds.), *Nuclear Spectroscopy of Astrophysical Sources*, AIP Conf. Proc. No. 170, p. 401.
Yoshimori, M.: 1989, *Space Sci. Rev.* **41**, 85.
Yoshimori, M. and Okudaira, K.: 1988, *Nucl. Instr. Meth.* **A272**, 880.
Yoshimori, M., Okudaira, K., Hirasima, Y., Yanagimachi, T., Kondo, I., Ohki, K., Watanabe, T., Nishimura, J., Yamagami, T., Murakami, T., Ito, M., and Yoshida, A.: 1988, *Nucl. Instr. Meth.* **A264**, 436.